Transformer spin-triplet superconductivity at the onset of isospin order in bilayer graphene

Zhiyu Dong, Andrey V. Chubukov, and Leonid Levitov

Phys. Rev. B **107**, 174512 — Published 11 May 2023

DOI: 10.1103/PhysRevB.107.174512

Transformer spin-triplet superconductivity at the onset of isospin order in bilayer graphene

Zhiyu Dong,[1] Andrey V. Chubukov,[2] and Leonid Levitov[1]

[1] *Department of Physics, Massachusetts Institute of Technology, Cambridge, MA 02139*
[2] *W. I. Fine Theoretical Physics Institute, University of Minnesota, Minneapolis, Minnesota 55455, USA*

(Dated: This manuscript was compiled on April 11, 2023)

We consider the origin of superconductivity found recently in Bernal bilayer graphene at the onset of isospin-polarized order. The superconductivity is induced by a parallel magnetic field and persists well above the Pauli limit, indicating an unconventional scenario of quantum-critical pairing, where soft fluctuations of isospin give rise to a spin-triplet superconductivity. We argue that the pairing interaction in this case is entirely repulsive, which stands in contrast to the typical quantum-critical pairing mechanisms. Superconductivity emerges through a "transformer" mechanism where the incipient valley polarization converts a frequency-independent repulsion into one with a strong non-monotonic frequency dependence in the presence of an in-plane magnetic field. Such interaction enables a non-zero solution for the pairing gap function that changes sign as a function of frequency. The same mechanism holds at zero fields in the presence of spin-orbit coupling, providing a likely explanation for the recently observed superconductivity in bilayer graphene on WSe_2 monolayer.

The quest for unconventional superconductivity (SC) governed by Coulomb repulsion rather than phonon attraction gained new momentum with the advent of graphene-based SC. In the SC phases found initially in moiré graphene [1–7], a flat-band system hosting strongly interacting electrons [8], delineating these mechanisms has proven to be a challenging task[9]. In some experiments, the SC appears to be clearly associated with correlated orders[6, 7, 10], suggesting non-phononic pairing scenarios[11–14]. Yet, other experiments report on SC that can be isolated (and thus decoupled) from other ordered phases[4, 15, 16], supporting phonon mechanism [17–19]. So far, no consistent picture has emerged, and presently, there is no clear verdict on the pairing mechanism. System complexity, such as the peculiar form of moiré flatband electron wavefunction[8, 20] and multiple kinds of moiré-related disorder, in particular the twist-angle disorder, strain, and buckling, make this debate difficult to settle.

Fortunately, recent research has uncovered two non-moiré systems that exhibit intertwined superconducting orders and correlated electronic orders — the field-biased Bernal bilayer graphene [21, 22] (BBG) and rhombohedral trilayer graphene [23, 24] (RTG). These systems present distinct benefits for studying strongly-correlated physics owing to the simplicity of their bandstructure and exceptional cleanness due to the absence of strain. It is noteworthy that superconducting phases are observed in both BBG and RTG systems in close proximity to interfaces between phases with different isospin polarization. The superconducting phases track these interfaces when the system parameters are being varied, see Fig.1.

Given these findings, it is almost inevitable to conclude that this behavior indicates presence of a pairing glue that is being mediated by a soft mode directly associated with isospin ordering. Interestingly, as discussed below, this pairing mechanism yields a superconducting phase near the onset of isospin polarization and general properties that closely match the observations. In particular, superconductivity appears at a finite in-plane magnetic field $B_\parallel$ and survives well beyond the Pauli limit, in agreement with the experiment. The superconductivity is spin-triplet, induced by a $B_\parallel$ that creates spin imbalance as shown in Fig.1 b) insets. Another interesting property that follows from this analysis is that, perhaps somewhat unexpectedly, the minority-spin carriers

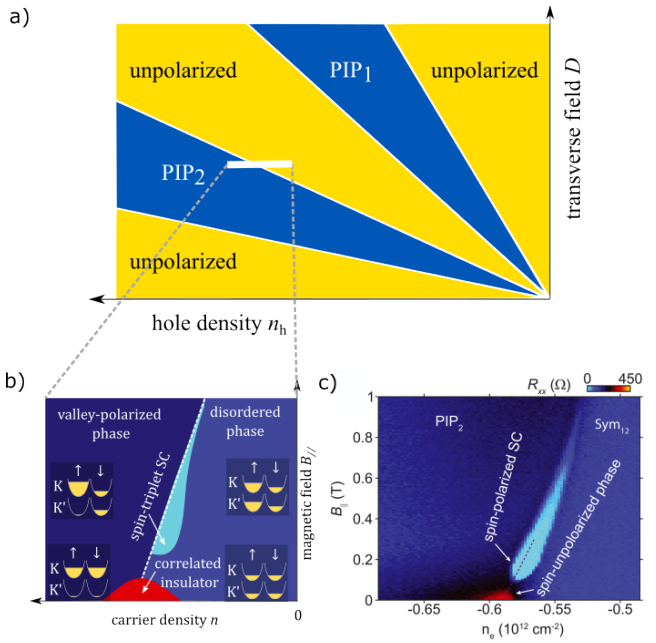

FIG. 1. a) Phase diagram schematic for isospin orders in BBG following Ref.[21]. In phases PIP_1 and PIP_2 only one and two isospin-polarized sub-bands are populated, respectively. Labels indicate isospin polarization in each phase at $B_\parallel = 0$. b) Predicted phase diagram for superconductivity governed by critical mode at the phase boundary between isospin-valley-polarized and unpolarized phases. Here ↑ and ↓ label spin-up (majority) and spin-down (minority) subbands, respectively. c) The measured phase diagram [21] strongly resembles the phase diagram predicted in b) [see text].

(spin-down in Fig.1) dominate pairing, whereas the contribution of the majority-spin carriers, despite a higher density, is negligible.

We stress that this pairing scenario is distinct from the existing mechanisms of pairing mediated by critical modes [25–32]. In previously studied instances of pairing near a quantum-critical point, soft quantum-critical modes associated primarily with spin fluctuations [33] generated an effective e-e attraction by exchange-type scattering of Cooper pairs either between different Fermi surfaces [34, 35] or between different hotspots on a single Fermi surface [36]. In graphene, to the contrary, the exchange component of (antisymmetrized) Coulomb interaction arising due to intervalley e-e scattering is weakened because the Fermi surface size in each valley is much smaller than the momentum transfer $\boldsymbol{K} - \boldsymbol{K}'$ for such e-e scattering processes. This renders pair scattering approximately valley-conserving, weakening the attractive exchange-type pairing interaction [37]. Likewise, the pair hopping interaction, known to be relevant for pairing in Fe-based materials, is absent in our case because in BBG the low-energy fermions are located near Dirac points $\boldsymbol{K}$ and $\boldsymbol{K}'$, but $2(\boldsymbol{K} - \boldsymbol{K}')$ is not a reciprocal lattice vector. As a result, the soft-mode-mediated pairing interaction, while being strong, is repulsive rather than attractive. Therefore, understanding this unusual superconductivity requires a mechanism that converts a strong repulsion mediated by the soft modes into an attraction.

Another clue comes from the observed unique dependence of T_c on a magnetic field $B_\parallel$: unlike textbook SC which is suppressed by a magnetic field, here SC is induced by $B_\parallel$ field. A finite threshold in $B_\parallel$ above which SC is observed (see Fig. 1c) suggests a pairing mechanism different from those studied in moiré [11–14] and RTG systems [23, 38, 39]. Since $B_\parallel$ only couples to spin when applied in-plane, the $B_\parallel$-induced SC indicates that spin imbalance is essential for pairing. Moreover, SC is found to persist in a high field, surviving well above the Pauli limit. The resilience of SC in a $B_\parallel$ field unambiguously points to a spin-triplet pairing and thus an unconventional pairing mechanism.

Here we demonstrate that superconducting pairing can be achieved through an attraction-from-repulsion scenario that ties together these key factors: a soft mode, repulsive Coulomb coupling, broken spin degeneracy, and pairing in the spin-triplet channel. The predictions of this scenario are in agreement with the observations [21]. In essence, at a finite $B_\parallel$, the pairing interaction, while remaining repulsive at all bosonic frequencies ν, becomes strongly retarded, thereby helping an effective attraction to emerge from bare repulsion. Namely, the pairing interaction acquires a non-monotonic frequency dependence for minority-spin carriers due to field-induced suppression of the pairing interaction at small ν. We show that this suppression is "universal," meaning it is not affected by the bandstructure, and enables the emergence of a superconducting state with a dispersive gap that changes sign as a function of frequency. The superconducting order parameter is of a spin-triplet and valley-singlet character, featuring an s-wave momentum dependence. The predicted critical temperature sharply peaks near the isospin polarization threshold. Similar scenarios for conventional s-wave pairing in the presence of strong repulsive Coulomb repulsion have been discussed repeatedly in the literature both early on [40–43] and recently [44–46].

We also investigate an alternative, yet closely associated, pairing mechanism, which involves majority-spin electrons subject to a finite $B_\parallel$. In this scenario, the pairing interaction between majority-spin electrons, governed by the soft mode, acquires a dependence on the soft-mode momentum arising due to the $2k_F$ singularity in polarization function. Under a parallel magnetic field the $2k_F$ values for the spin-up and spin-down Fermi seas become unequal and, as a result, the pairing interaction for the majority-spin Fermi sea is modulated by the strength of the $B_\parallel$ field. This interaction induces an attraction in non-s-wave channels via the Kohn-Luttinger (KL) mechanism [47]. As a result, we obtain pairing in a spin- and valley-triplet, p-wave channel.

Pairing in either the minority-spin or majority-spin channel accounts for all the salient features observed in the experimentally determined phase diagram in BBG [see Fig.1 c)]: First, superconductivity occurring at a phase boundary is natural for a scenario that relies on critical isospin modes. Second, the predicted superconductivity has a threshold in $B_\parallel$ field as a finite $B_\parallel$ is required to overcome bare repulsion. At a lower $B_\parallel$, we predict a strong repulsive interaction. This interaction is expected to produce a correlated insulator state, in line with the observations [Fig.1 c)].

Another aspect of the measured phase diagram that supports this scenario is the dependence of the onset of the isospin order (PIP_2 order in the notations of [21]). In experiment [21], the $B_\parallel$ field merely pushes the onset of the order to lower carrier densities, producing a phase boundary with a constant slope marked by the dashed line in Fig.1 c). As we will see, this behavior follows directly from our model (see Eq.(34) below and accompanying discussion). We note that in Fig.1 c), borrowed from the experimental work [21], the x axis is drawn from high carrier density to low carrier density. The experimental and theoretical slopes of the phase boundary match both in sign and value, lending further support to the theory.

Further support for this mechanism comes from a recent experiment [22] that reports the observation of superconductivity in a BBG placed on top of a monolayer of WSe2. In this system, superconductivity arises even when the magnetic field strength $B_\parallel$ is zero, and persists even when $B_\parallel$ values exceed the Pauli limit. This behavior can be explained within the same framework as described above by considering the influence of interfacial spin-orbit coupling (SOC) induced in graphene due to the presence of WSe_2. Such SOC effectively induces a valley-odd Zeeman field, which acts for SC in the same way as the magnetic field $B_\parallel$. Naturally, at a finite $B_\parallel$

the actual and effective B fields combine to induce SC above the Pauli limit. Further details of this scenario are discussed in Sec.VII.

I. PAIRING NEAR THE ONSET OF VALLEY POLARIZATION

Motivated by the observed relation between valley polarization instability and the emergence of superconductivity, here we employ a minimal model for the former and discuss its implications for the latter. We consider susceptibilities for the valley and spin imbalances, the quantities that diverge near the onset of valley or spin polarization. These quantities can be linked to the free-fermion density-density response function in a standard manner. With this framework established, we are able to investigate the "transformer" pairing glue that emerges at the onset of instability, and analyze its distinctive characteristics and the properties of the resulting superconducting state.

First, we describe the hierarchy of energy scales in our problem. In the regime where superconductivity occurs, the bandgap created by the displacement field is approximately 100 meV [21]. Bandstructure calculations [48, 49] predict a Fermi energy of roughly 10 meV at the carrier density and D field values where superconductivity occurs. This Fermi energy is much smaller than the bandgap of D. The electron-electron interaction energy is expected to be comparable to the Fermi energy, as the system is close to an isospin Stoner instability. The experiment reports a relatively small superconducting transition temperature (T_c) of 30 mK, which is comparable to the minimal Zeeman energy $\approx 1\times10^{-2}$ meV required to create superconductivity upon increasing $B_\parallel$[21]. Since this value is much smaller than the interaction and kinetic energies, we will ignore the Zeeman energy at first and account for it perturbatively later.

We model the interacting electrons in BBG using a short-range interaction

$$H=\sum_i \epsilon_i(\boldsymbol{p})\psi^\dagger_{i\boldsymbol{p}}\psi_{i\boldsymbol{p}}+\sum_{ii'}\frac{V_0}{2}\psi^\dagger_{i\boldsymbol{p}+\boldsymbol{q}}\psi^\dagger_{i'\boldsymbol{p}'-\boldsymbol{q}}\psi_{i'\boldsymbol{p}'}\psi_{i\boldsymbol{p}}, \quad (1)$$

where $i,i'=\boldsymbol{K}\uparrow,\boldsymbol{K}\downarrow,\boldsymbol{K}'\uparrow,\boldsymbol{K}'\downarrow$ are isospin indices. A single-band model $\epsilon_i(\boldsymbol{p})$ will be used as a proxy for a more realistic Dirac band. This single-band model Eq.(1) is obtained by projecting the two-band model of BBG[48, 49] on the conduction band, which in the regime of $D\gg E_F$ is well isolated from the valence band. This band projection in general yields wavefunction formfactors $\langle u_p|u_{p+q}\rangle$, where $|u_p\rangle$ is the cell-periodic part of the Bloch function. In Eq.(1), we take the form factors to be unity, as appropriate for the case $D\gg E_F$ [50]. Indeed, for the states obtained from a simple two-band Hamiltonian [48, 49] the formfactors at small energies $E_F\ll D$ are close to unity, with the deviation being as small as E_F/D. Therefore, Eq.(1) provides a reasonable approximation so long as $D\gg E_F$, regardless of the bandstructure details such as the trigonal warping[48, 49].

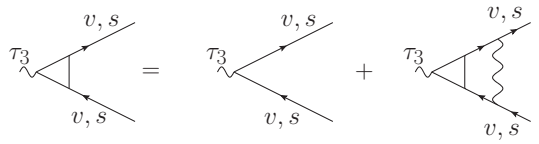

FIG. 2. Ladder diagrams describing the valley-polarization instability in a mean-field approximation. Here v and s are valley and spin indices $\boldsymbol{K}$, $\boldsymbol{K}'$ and $\uparrow,\downarrow$ The lines with arrows represent Green's functions, the wavy line is the electron-electron interaction, vertices represent the τ_3 Pauli matrix in valley subspace. No summation over v and s is assumed.

In Eq.(1), the momentum-independent electron-electron interaction V_0 represents a repulsion short-ranged as compared to Fermi wavelength. This interaction mimics Coulomb $1/r$ interaction screened out at momentum transfers smaller than $2k_F$, taken here as an estimate for the screening parameter in the Thomas-Fermi model. Eq.(1) only accounts for the intravalley scattering processes. The inter-valley carrier scattering processes mediated by the $1/r$ interaction can be ignored because the $1/r$ interaction form factor drops rapidly for momentum transfers $2k_F<q<q_{\max}\sim|\boldsymbol{K}-\boldsymbol{K}'|$, where the ratio $q_{\max}/2k_F$ can be as large as a 100 for BBG.

In the graphene bilayer, an isospin-polarization in the valley (τ) and spin (σ) subspaces can conceivably occur through various routes, with the main scenarios being:

1. A $q=0$ instability towards valley-only polarization ($M=\tau_3$, σ_0)
2. A $q=0$ instability towards intra-valley ferromagnetism (FM) ($M=\tau_0\pm\tau_3$, σ_n)
3. An instability with momenta $\boldsymbol{K}-\boldsymbol{K}'$ in either charge channel ($\tau_\pm$, σ_0) or spin channel ($M=\tau_\pm$, σ_n) (see e.g. Refs.[51, 52]).

Matrices M in spin/valley space describe the orders through a spontaneously generated fictitious field term in the Hamiltonian,

$$\delta H=\sum_{\boldsymbol{p}i}\psi^\dagger_{i\boldsymbol{p}}M_{ii'}\psi_{i'\boldsymbol{p}}, \quad (2)$$

where i, i' label spin and valley degrees of freedom. Here τ_m and σ_n $(m,n=0,1,2,3)$ are valley and spin Pauli matrices, and σ_0 is the identity 2×2 spin matrix. In our simplified model, we find that these instabilities are degenerate. However, in a more realistic scenario involving a generic interaction, one of the instabilities will typically dominate and lift the degeneracy (as discussed below). Experiments identified the ordered phase PIP_2 with a valley-imbalanced phase [21]. We therefore will focus on the τ_3 valley polarization instability, and defer a discussion of potential superconductivity near other instabilities to a later point.

An instability towards valley polarization, described by the $M = \tau_3$ matrix, can be represented diagrammatically, as shown in Fig.2, where arrows represent the electron Green's functions $G_s(\omega, \boldsymbol{p}) = 1/(i\omega - \epsilon_s(\boldsymbol{p}))$ and the wave lines represent the interaction. Summing up ladder diagrams in the τ_3 channel yields a standard Stoner-like condition for the instability threshold (see e.g. Ref.[51]):

$$V_0\Pi_{3,s} = -1, \quad \Pi_{3,s} = \frac{1}{2}\sum_{\omega,\boldsymbol{p}} \mathrm{tr}\left(\tau_3\mathcal{G}_s(\omega,\boldsymbol{p})\tau_3\mathcal{G}_s(\omega,\boldsymbol{p})\right). \tag{3}$$

where the quantity $\Pi_{3,s}$ denotes the polarization in the valley channel. Here $s =\uparrow,\downarrow$ denotes electron spin, tr is a valley trace involving summation over valley indices, with the spin indices not being summed over. The quantities $\mathcal{G}_s(\omega,\boldsymbol{p})$ are Green's functions of spin-s electrons, each being a 2×2 matrix in valley space:

$$\mathcal{G}_s(\omega,\boldsymbol{p}) = \begin{pmatrix} G_{Ks}(\omega,\boldsymbol{p}) & 0 \\ 0 & G_{K's}(\omega,\boldsymbol{p}) \end{pmatrix}. \tag{4}$$

In our notations, $\Pi_{3,s}$ is negative, so the instability develops at a positive V_0. The corresponding valley-polarization susceptibility is

$$\chi_{v,s} = \frac{\Pi_{3,s}}{1 + V_0\Pi_{3,s}}, \tag{5}$$

where the subscript v stands for valley polarization. It follows directly from Eq.(3) that the free-fermion polarization functions obey

$$\Pi_{3,s} = \Pi_s^K = \Pi_s^{K'}, \tag{6}$$

where $\Pi_s^v = \sum_{\omega,p} G_{vs}(\omega,p)G_{vs}(\omega,p)$, $v = \boldsymbol{K}$, $\boldsymbol{K'}$ is the bare polarization bubble (bare susceptibility) in valleys $\boldsymbol{K}$ and $\boldsymbol{K'}$. The identity $\Pi_s^K = \Pi_s^{K'}$ follows from the mirror symmetry that maps valleys $\boldsymbol{K}$ and $\boldsymbol{K'}$ on each other. Due to this symmetry, the free-fermion dispersion behaves as $\epsilon(\boldsymbol{K}+\boldsymbol{p}) = \epsilon(\boldsymbol{K'}-\boldsymbol{p})$, and, therefore, $\Pi_s^K = \Pi_s^{K'}$. Below we suppress the valley index, i.e., replace Π_s^K and $\Pi_s^{K'}$ by just Π_s. For free electrons with parabolic dispersion and at a zero magnetic field, $\Pi_s = -\nu$, where ν is the density of states at $\epsilon = \epsilon_F$ for one isospin species.

We emphasize that while the valley susceptibility diverges, the ordinary charge susceptibility $\chi_{c,s}$, obtained by the ladder summation similar to that in Fig.2, but with τ_3 replaced with an identity matrix and the interaction being a sum of the Hartree and Fock contributions, shows no divergence. Explicit calculation yields

$$\chi_{c,s} = \frac{\Pi_s}{1 + V_0\Pi_s - 2\sum_{s'} V_0\Pi_{s'}}. \tag{7}$$

The factor of 2 before the summation over spin s' is due to the two-fold valley degeneracy (see Eq.(6)). At zero magnetic field, where $\Pi_s = \Pi$, this reduces to

$$\chi_{c,s} = \frac{\Pi}{1 - 3V_0\Pi}, \tag{8}$$

where the factor $3 = 4 - 1$ arises as a combination of the Hartree and Fock terms in Eq.(7). The Hartree term is four times greater than the Fock term and is of the opposite sign, which suppresses the charge instability.

At a non-zero magnetic field, the values $\Pi_\uparrow$ and $\Pi_\downarrow$ are different, and the analysis requires more care. Performing the same computation as above and noting that, in the calculation, the $\uparrow$ and $\downarrow$ spin components decouple, and Eq. (5) holds. Then valley instability for spin $\uparrow$ occurs at $V_0\Pi_\uparrow = -1$, whereas for spin $\downarrow$ it occurs at $V_0\Pi_\downarrow = -1$. In experiment [21], valley polarization is pushed to a lower density at an increasing $B_\parallel$ field [see Fig.1 c)]. Comparing this to the Stoner instability picture indicates that criticality in a finite $B_\parallel$ is linked to the majority-spin carriers. In our model, this implies that $|\Pi_\uparrow| > |\Pi_\downarrow|$, and the leading instability occurs at $V_0\Pi_\uparrow = -1$.

With the valley polarization instability framework established, we proceed to discuss how the attraction-from-repulsion pairing mechanism arises at the onset of valley polarization. It is instructive to outline the physics of this mechanism before proceeding with calculations. In the presence of a magnetic field, valley polarization first emerges for spin-up (majority-spin) carriers. This makes spin-up valley-polarizing excitations gapless, whereas excitations in spin-down (minority-spin) Fermi seas remain gapped. Softening of valley-polarizing modes leads to a vanishing of $1 + V_0\Pi_\uparrow$, while $1 + V_0\Pi_\downarrow$ remains finite. These two combinations appear in equal-spin pairing vertices $\Gamma_{s,s}$ as $\Gamma_{\uparrow,\uparrow} \propto 1/(1 + V_0\Pi_\uparrow)$ and $\Gamma_{\downarrow,\downarrow} \propto (1 + V_0\Pi_\uparrow)/(1 + V_0\Pi_\downarrow)^2$.

These quantities, which describe superconductivity in the spin-up and spin-down channels, have a very different behavior at the valley polarization instability. The pairing vertex for spin-up carriers, $\Gamma_{\uparrow,\uparrow}$, diverges at the transition. However, it is of a repulsive sign and monotonically decreases with frequency. For such a vertex, the superconductivity selfconsistency equation has no non-zero solution for the gap function. However, the quantity $\Gamma_{\downarrow,\downarrow}$ shows a different behavior because of the factor $1 + V_0\Pi_\uparrow$ that vanishes near the instability. This gives a negative feedback effect on $\Gamma_{\downarrow,\downarrow}$ and, as a result, this quantity is substantially reduced at small frequencies. The frequency dependence of $\Gamma_{\downarrow,\downarrow}$ then becomes non-monotonic, dropping from more repulsive at high frequencies to less repulsive at low frequencies. This frequency dependence, despite the positive sign of $\Gamma_{\downarrow,\downarrow}$, allows spin-down electrons to form spin-triplet Cooper pairs with a sign-changing gap function $\Delta(\omega)$.

Below we first discuss the pairing interaction at a zero magnetic field $B_\parallel = 0$, where $\Pi_{s=\uparrow} = \Pi_{s=\downarrow} = \Pi$ (see Sec.II), and then extend the results to finite $B_\parallel$, where $\Pi_{s=\uparrow} \neq \Pi_{s=\downarrow}$ and the frequency dependence of the pairing interaction becomes nonmonotonic, leading to superconductivity (see Sec.III).

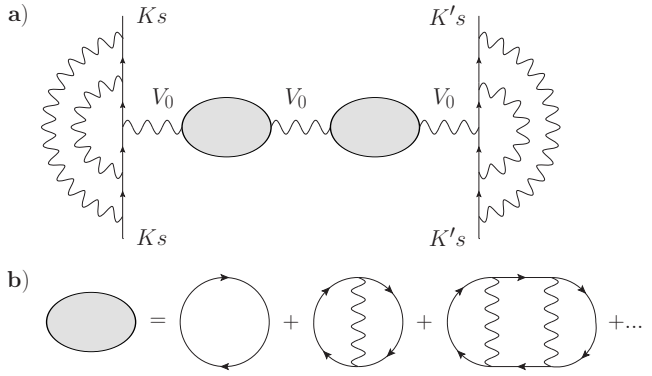

FIG. 3. a) Diagrams describing the effective pairing interaction between electrons in valleys $\boldsymbol{K}$ and $\boldsymbol{K}'$ mediated by quantum-critical modes, Eq.(11). These processes give a divergent enhancement to forward scattering near the valley-polarization instability (see text). b)The diagrammatic representation of the irreducible part of the charge susceptibility $\chi_{c,s}$ (the shaded ellipse), summed over $s =\uparrow,\downarrow$.

II. REPULSION AT $B_\parallel = 0$

It is instructive to start with $B_\parallel = 0$. In this case, the pairing interaction is repulsive and has a monotonic frequency dependence. This behavior, which is incompatible with pairing, will be contrasted in Sec.III with that arising at a finite $B_\parallel$, where the interaction remains repulsive but acquires a non-monotonic frequency dependence that leads to pairing.

We start by noting that the pairing interaction with zero total momentum occurs between fermions in different valleys, $\boldsymbol{K}$ and $\boldsymbol{K}'$. At the lowest order, the pairing interaction is just V_0, however near the onset of the valley polarization order dressing it with soft modes becomes essential. We argue below that the relevant dressing is the one illustrated in Fig.3. The unique property of this dressing is that it enhances the pairing interaction by a large factor $1/(1 + V_0\Pi)$. We proceed by analyzing how these diagrammatic series shown in Fig.3 emerge in order-by-order expansion in V_0.

To understand the pairing, we need to compute the irreducible vertex function in the pairing channel, $\Gamma_{ss'}$. By general rules, $\Gamma_{ss'}$ is a fully dressed antisymmetrized interaction describing scattering between fermion pair states $(\boldsymbol{k}, -\boldsymbol{k}) \to (\boldsymbol{p}, -\boldsymbol{p})$. The specifics of our case are that (i) pairing involves one fermion near $\boldsymbol{K}$ and one near $\boldsymbol{K}'$, and (ii) the scattering between $\boldsymbol{K}$ and $\boldsymbol{K}'$ is weak in graphene and can be neglected. In this situation, the contributions to Γ_{ss} from antisymmetrization vanish, $\Gamma_{s,s'}$ becomes spin-independent $\Gamma_{s,s'} = \Gamma$ and we only need to analyze how the direct pairing interaction V_0 is being dressed.

To second-order in V_0, we have three topologically different diagrams shown in Fig.4. The first two diagrams [see panels a) and b)] are known as bubble and "wine glass" diagrams. Since the two intermediate electron lines in each of these two diagrams are from the same valley, their contributions are the same as from irreducible processes in Fig. (2) – the ones which give rise to valley polarization. In comparison, the last diagram, known as the "exchange" diagram, contains two intermediate electron lines in which one is from valley $\boldsymbol{K}$, whereas the other is from valley $\boldsymbol{K}'$ [see panel c)]. Its contribution is not directly related to the processes leading to valley polarization. Because our goal is to analyze how the pairing interaction evolves near the onset of valley polarization, we focus on the diagrams with a leading-order divergence. We, therefore, neglect the "exchange" diagrams at each order of expansion in V_0 and include only the bubble and "wine glass" diagrams (see Ref. [53] for similar consideration). Some examples of the leading-order diagrams at a 3-loop order are shown in Fig.5 a). These are diagrams with zero, one, and two bubbles. In comparison, several typical subleading diagrams at a 3-loop order are shown in Fig.5 b).

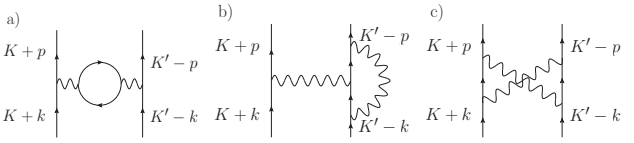

FIG. 4. Three types of second-order diagrams: a) bubble diagram; b) "wine glass" diagram; c) "exchange" diagram.

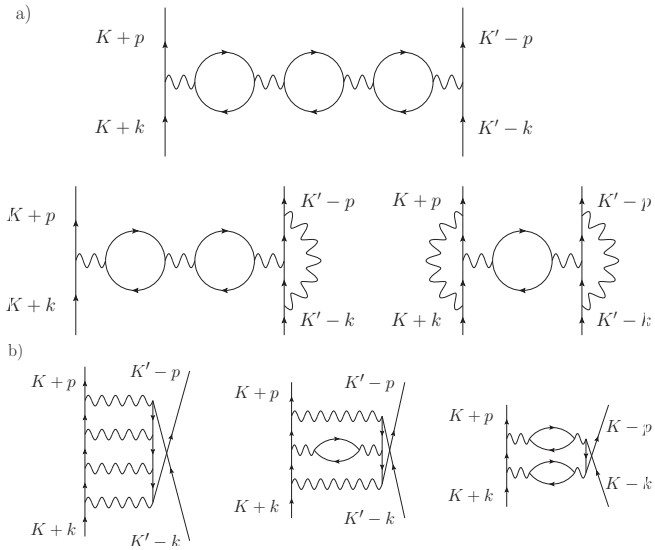

FIG. 5. Diagrams at 3-loop order: a) diagrams with 3 bubbles that are maximally divergent near the Stoner instability; b) diagrams with 0, 1, and 2 bubbles, which are subleading at the Stoner instability.

The sum of the bubble and wine glass diagrams can be rewritten as illustrated in Fig.3. Below, we work out the analytical expression. First, diagrams without bubbles sum up into $V_0\gamma^2$, where

$$\gamma = \frac{1}{1 + V_0\Pi}. \tag{9}$$

We next account for the polarization bubbles. Insertion of one bare bubble contributes the factor $-4V_0\Pi$, where -1 is due to a fermionic loop and the factor of 4 arises due to spin and valley degeneracy. An insertion of ladder series of interactions into each bubble further converts Π into fully dressed irreducible $\Pi\gamma$. The resulting effective interaction described by these diagrams can thus be written as

$$\Gamma = \gamma^2 \frac{V_0}{1 - 4V_0\Pi\gamma} \tag{10}$$

$$= \frac{V_0}{(1 + V_0\Pi)(1 - 3V_0\Pi)}. \tag{11}$$

This vertex function contains the factor $1/(1+V_0\Pi)$ and hence it gets enhanced near the onset of valley polarization. Near $V_0\Pi = -1$, it can be approximated as

$$\Gamma \approx \frac{V_0}{4} \frac{1}{1 + V_0\Pi}. \tag{12}$$

Still, the interaction remains positive-valued, i.e., repulsive. This behavior is distinct from that found for pairing mediated by a critical $q = 0$ mode in other systems, such as a nematic QCP[25–27]. Indeed, in these systems electrons with $\mathbf{k}$ and $-\mathbf{k}$ live on the same Fermi surface and interact through exchange processes. In our case, such a process is forbidden as it requires a fermion to scatter from one valley to the other.

For a more accurate treatment, we should take into consideration the fact that the valley polarization instability is the one with zero momentum transfer ($\boldsymbol{q} = 0$) and zero frequency transfer ($\nu = 0$). At a finite $\boldsymbol{q}$ and a finite ν, the polarization Π becomes the function of both, $\Pi = \Pi(\nu, \boldsymbol{q})$, and the vertex Γ also becomes $\Gamma(\nu, \boldsymbol{q})$. The static polarization bubble is a regular function of q^2 and the dominant contribution to the dynamical part comes from the Landau damping (see e.g. Ref.[43]). Then

$$1 + V_0\Pi(\nu, \boldsymbol{q}) \approx \frac{|\nu|}{v_F q} + Kq^2 + \delta, \tag{13}$$

where $\delta = 1 + V_0\Pi(0, 0)$ characterizes a detuning from the valley-polarization phase boundary. The stiffness parameter K and the Fermi velocity v_F are determined by band dispersion $\epsilon(\boldsymbol{p})$. In writing the Landau damping term, we assumed that $|\nu| \ll v_F q$. Plugging this $\Pi(\nu, q)$ into Eq.(12) we obtain the vertex $\Gamma(\nu, \boldsymbol{q})$ at small $\boldsymbol{q}$ and ν in the form

$$\Gamma(\nu, \boldsymbol{q}) = \frac{V_0}{4} \frac{1}{\frac{|\nu|}{v_F q} + Kq^2 + \delta}. \tag{14}$$

This effective interaction with the dynamical Landau-damping term is similar to the one studied in the context of quantum-critical pairing in metals on the verge of an Ising-nematic or Ising-ferromagnetic instability [29, 31, 54] and for 2D fermions coupled to emerging gauge field in a doped Mott insulator [55–59]. However, the sign of the interaction in our case is repulsive, and it monotonically decreases with frequency. Such an interaction does not lead to superconductivity.

III. ATTRACTION FROM REPULSION AT $B_\parallel \neq 0$

Here we consider how the pairing interaction, Eq.(14), is altered at $B_\parallel \neq 0$. We show that, while it remains repulsive, it becomes non-monotonic in frequency for fermions with spin direction opposite to the field. This leads to pairing for minority-spin carriers, as we demonstrate.

At a finite $B_\parallel$, the polarization bubble Π_s does depend on spin $s = \uparrow, \downarrow$ and this has to be included in the calculation of the pairing vertex $\Gamma_{s,s'}$. We will focus on equal-spin channel $s = s'$. Repeating the same calculations as above, but keeping the dependence on s in Π_s, we obtain

$$\Gamma_{s,s} = V_0\gamma_s^2 \frac{1}{1 - 2V_0 \sum_{s'} \Pi_{s'}\gamma_{s'}}, \tag{15}$$

where $\gamma_s = 1/(1 + V_0\Pi_s)$. This can be re-expressed as

$$\Gamma_{s,s} = \frac{(1 + V_0\Pi_\uparrow)(1 + V_0\Pi_\downarrow)V_0}{(1 + V_0\Pi_s)^2 \left[1 - V_0 \left(\Pi_\uparrow + \Pi_\downarrow\right) - 3V_0^2\Pi_\uparrow\Pi_\downarrow\right]}. \tag{16}$$

As before, each polarization bubble is a function of ν and $\boldsymbol{s}$, such that

$$1 + V_0\Pi_s(\nu, \boldsymbol{q}) \approx \frac{|\nu|}{v_F q} + Kq^2 + \delta_s, \tag{17}$$

Here and below, for simplicity, we take the Fermi velocities and the stiffness parameters for both spin species to be equal, $v_{F,\uparrow} = v_{F,\downarrow} = v_F$, $K_\uparrow = K_\downarrow = K$. The quantities $\delta_{s=\uparrow,\downarrow}$, which define the detuning from the phase boundary, are equal in the absence of $B_\parallel$-induced Zeeman interaction but become unequal when $B_\parallel \neq 0$. Comparing the two denominators in Eq.(16), we find that the leading instability in a magnetic field occurs at either $V_0\Pi_\uparrow = -1$ or $V_0\Pi_\downarrow = -1$. As discussed in Sec.I, experiments indicate [21] that criticality at a finite $B_\parallel$ occurs first for majority-spin carriers. This translates into $\delta_\uparrow = 0$ at the onset of valley polarization, whereas $\delta_\downarrow$ remains finite. As a result, $V_0\Pi_\uparrow \approx -1$, and in the right-hand side of Eq.(16), $1 - V_0 \left(\Pi_\uparrow + \Pi_\downarrow\right) - 3V_0^2\Pi_\uparrow\Pi_\downarrow \approx 2(1 + V_0\Pi_\downarrow)$. As a result,

$$\Gamma_{\uparrow,\uparrow} \approx \frac{V_0}{2} \frac{1}{1 + V_0\Pi_\uparrow} = \frac{V_0}{2} \frac{1}{\frac{|\nu|}{v_F q} + Kq^2 + \delta_\uparrow}, \tag{18}$$

and

$$\Gamma_{\downarrow,\downarrow} \approx \frac{V_0}{2} \frac{1 + V_0\Pi_\uparrow}{(1 + V_0\Pi_\downarrow)^2} = \frac{V_0}{2} \frac{\frac{|\nu|}{v_F q} + Kq^2 + \delta_\uparrow}{(\frac{|\nu|}{v_F q} + Kq^2 + \delta_\downarrow)^2}. \tag{19}$$

Both vertices remain positive (repulsive), but they now have qualitatively different frequency dependence: $\Gamma_{\uparrow\uparrow}$ is similar to that found for $B_\parallel = 0$, and is monotonically decreasing with ν. On the contrary, the pairing interaction for minority-spin electrons $\Gamma_{\downarrow\downarrow}(\nu, q)$ has a non-monotonic frequency dependence because at small momentum $q \ll \sqrt{\delta/K}$, it is strongly suppressed at low frequencies $\nu < v_F|q|\delta_\downarrow$ and not suppressed at $\nu > v_F|q|\delta_\downarrow$.

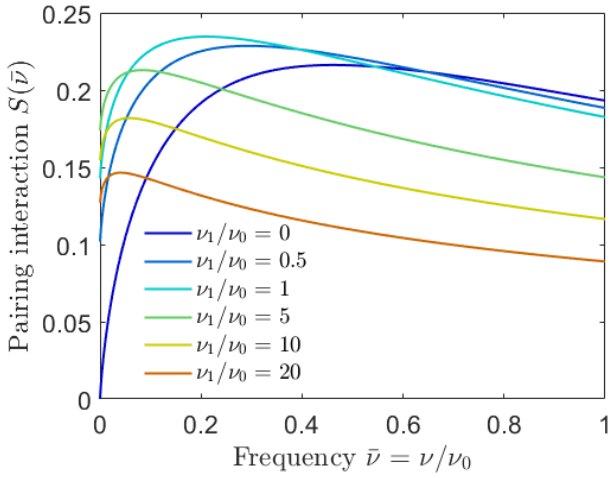

FIG. 6. Frequency-dependent pairing interaction $S(\bar{\nu})$, Eq. (23), describing the universal contribution of a soft mode. The non-monotonic frequency dependence, which is a generic property of $S(\bar{\nu})$ for all values of the stiffness K, allows for a repulsive interaction to generate an attractive effective pairing interaction. The value at $\nu = 0$ is finite at $K > 0$ and zero at $K = 0$. In the latter case superconducting T_c is non-zero for any $\delta_\downarrow$, the detuning from the critical point for spin-down fermions.

Then $\Gamma_{\downarrow\downarrow}$ increases at low frequencies and decreases at higher frequencies.

The s-wave component of this vertex (by far the largest one for small Fermi pockets, $2k_F \ll |\boldsymbol{K} - \boldsymbol{K}'|$) is the average of $\Gamma_{\downarrow\downarrow}(\nu, q)$ over the momentum transfers on the Fermi surface $\overline{\Gamma}_{\downarrow\downarrow}(\nu) = 2\int_0^{\sim k_F} \frac{dq}{2\pi}\Gamma_{\downarrow\downarrow}(\nu, q)$. This quantity can be cast into a scaling form

$$\overline{\Gamma}_{\downarrow\downarrow}(\nu) = \frac{V_0 k_F}{2\pi\delta_\downarrow} S\left(x, x_1\right), \quad x = \frac{\nu}{\nu_0}, \quad x_1 = \frac{\nu_1}{\nu_0}, \tag{20}$$

where $\nu_0 = E_F\delta_\downarrow$, $\nu_1 = E_F K k_F^2$, and $E_F = v_F k_F$. At $\nu_1 \ll \nu_0$, the function

$$S(x, 0) = x\left(\log\frac{1+x}{x} - \frac{1}{1+x}\right) \tag{21}$$

is manifestly non-monotonic: it increases with x at small x, passes through a maximum at $x \sim 0.5$, and drops at higher x. We emphasize that the non-monotonic behavior is fully induced by $B_\parallel$, which splits $\delta_\uparrow$ and $\delta_\downarrow$. The non-monotonic dependence holds if we increase the ratio ν_1/ν_0 as illustrated in Fig.6.

Below we solve the gap equation to demonstrate that a non-monotonic frequency dependence of $\overline{\Gamma}_{\downarrow\downarrow}(\nu)$ leads to pairing between spin-minority carriers at a non-zero T_c. The gap function is s-wave and changes sign as a function of frequency. For majority-spin carriers, the interaction is monotonic in frequency [see Eq.(18)] and does not give rise to pairing. As a result, in some range of $T < T_c$, the system simultaneously hosts both metallic carriers and superconducting pairs, unless a magnetic scattering is introduced. The coexistence of two types of carriers can be probed by searching for in-gap states in tunneling spectroscopy due to metallic carriers.

We note the decoupling between fermions with opposite spins no longer holds in a general setting. As we will see later in Sec.V, in a generalized model, pairing susceptibilities for spin-up and spin-down fermions are coupled. In this case, the development of a superconducting gap for minority-spin carriers generates a smaller, but finite gap for majority-spin carriers. Still, tunneling experiments should reveal states with energies between smaller and larger gaps.

IV. SOLVING THE GAP EQUATION

The superconducting gap equation for the pairing of spin-down fermions, mediated by $\overline{\Gamma}_{\downarrow\downarrow}(\nu)$, is

$$\Delta(\omega) = -\frac{T_c}{2v_F}\sum_{\omega'=\pi T_c(2n+1)}\frac{\Delta(\omega')\overline{\Gamma}_{\downarrow\downarrow}(\omega-\omega')}{|\omega'|}, \tag{22}$$

The overall minus sign reflects that the interaction is repulsive. The gap equation takes a universal form when expressed in terms dimensionless $\bar{T}_c = T_c/\nu_0$ and $\bar{\omega} = \omega/\nu_0$:

$$\Delta(\bar{\omega}) = -\lambda\pi\bar{T}_c\sum_{\bar{\omega}'=\pi\bar{T}_c(2n+1)}\frac{\Delta(\bar{\omega}')}{|\bar{\omega}'|}S\left(\bar{\omega}-\bar{\omega}', 0\right) \tag{23}$$

where $\lambda = k_F V_0/(4\pi^2 v_F\delta_\downarrow)$. Because $S\left(\bar{\omega}-\bar{\omega}', 0\right)$ is strongly peaked at $|\bar{\omega}-\bar{\omega}'| = \bar{\nu}_* \approx 0.5$, one can change the overall sign in Eq.(23) by searching for gap functions which change sign under $\bar{\omega} \to \bar{\omega} + \bar{\nu}_*$. At small λ, analytical consideration yields $T_c \propto \omega_0 e^{-1/\lambda^2}$ (Ref. [45]). At $\lambda \leq 1$, $T_c \sim \omega_0$, but with a numerically small prefactor. At larger λ, the prefactor increases and at $\lambda \gg 1$ (i.e., at small $\delta_\downarrow$), $T_c \sim \lambda\nu_0 \sim E_F$.

For completeness, the analysis of the pairing problem at large λ must also include fermionic selfenergy. This is required because the pair-breaking effect due to self-energy may suppress superconductivity. To gain insight, one can start with the intravalley analog of the leading-order diagrams for the pairing interaction $\Gamma_{\downarrow\downarrow}(\nu, q)$ pictured in Fig.3. Replacing fermions in different valleys with fermions in identical valleys yields a divergent contribution to the intra-valley interaction, which, in turn, produces a large contribution to the selfenergy. Does this imply that near Stoner instability the selfenergy diverges in the same way as the pairing interaction and, through pair-breaking effects, can suppress pairing?

This concern turns out to be unfounded because, for an intravalley interaction, focusing solely on the intravalley analogs of the diagram in Fig.3 is not justified. One must also consider other diagrams that are allowed for intravalley scattering. The contributions of these diagrams tend to suppress the divergence of the effective

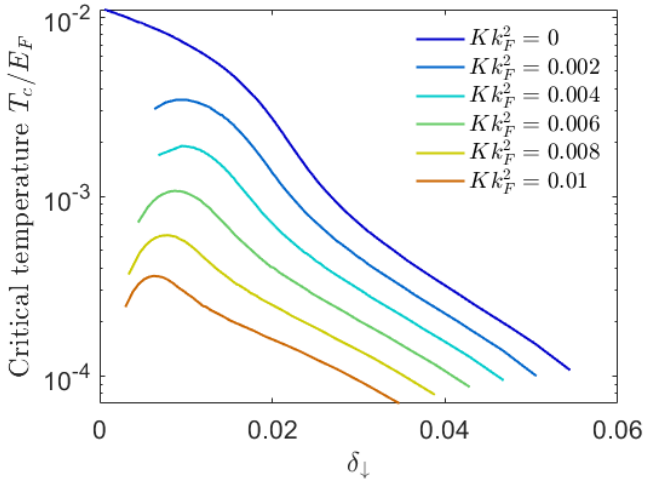

FIG. 7. Critical temperature T_c vs. the detuning from criticality $\delta_\downarrow$ for spin-down carriers, a parameter controlled by $B_\parallel$. For $K = 0$, T_c is finite for all δ. For $K \neq 0$, to the contrary, each curve starts at a finite threshold value $\delta_\downarrow > 0$. As K grows, the threshold value first grows and then decreases, reflecting the behavior of $S(\nu)$ at small ν shown in Fig.6 (see text).

interaction at Stoner instability. In particular, the "exchange" processes pictured in Fig.4 c) that were negligible for the inter-valley pairing interaction [see Sec.II] , can contribute to the intra-valley density-density interaction and impact the selfenergy. However, when these diagrams are accounted for, every time we draw a bubble, we must add to it an "exchange" contribution that looks like Fig.4 c). These "exchange" diagrams tend to cancel the contributions from the bubbles since these two types of diagrams differ by a sign arising from a fermionic loop. As a result, the intra-valley interaction that dominates the selfenergy does not diverge at the Stoner instability as strongly as the pairing interaction $\Gamma_{\downarrow\downarrow}$ does.

Furthermore, in AppendixA we analyze the impact of the selfenergy on T_c in a different way. We obtain the selfenergy accounting only for the intravalley analog of the diagram in Fig.3. This method, as argued above, grossly overestimates the selfenergy. Nevertheless, we find T_c values that are still acceptable. This observation further justifies ignoring selfenergy in our analysis.

Critical temperature values T_c, obtained by numerical solution of Eq. (23), are shown in Fig.7. We set $k_F V_0/(2\pi v_F) = 1$, as required for a Stoner instability, and set $E_F = 10$meV. We see that at $\nu_1 = 0$, T_c monotonically increases with decreasing $\delta_\downarrow$ and at small $\delta_\downarrow$ saturates at roughly 1K.

For a more realistic case of $\nu_0 \sim \nu_1$, the momentum-averaged $\overline{\Gamma}_{\downarrow\downarrow}(\nu)$ tends to a finite value at $\nu = 0$, leading to a smaller T_c and also setting a threshold on $\delta_\downarrow$ as an s-wave pairing by a frequency-dependent repulsion is a threshold phenomenon [44–46], and at a small $\delta_\downarrow$ the non-monotonicity of $\overline{\Gamma}_{\downarrow\downarrow}(\nu)$ is too weak to give rise to a pairing when the self-energy is included. At larger $\delta_\downarrow$ T_c also drops because the coupling λ gets smaller. This gives rise to a dome-like dependence of T_c on $\delta_\downarrow$ at a given Kk_F^2 value. For $Kk_F^2 = 10^{-2}$ we obtained at $T_c \sim 35$mK at optimal $\delta_\downarrow = 7 \times 10^{-3}$. This value is in line with experimental T_c.

V. ROBUSTNESS OF THE TRANSFORMER PAIRING MECHANISM

To test the robustness of the attraction-from-repulsion pairing mechanism, here we demonstrate that the non-monotonic frequency dependence of the pairing interaction, a property central to our pairing mechanism, is a general behavior. To this end, we analyze a generalized model where different types of isospin instabilities are non-degenerate.

As a reminder, as stated in the Introduction, the minimal model we studied above does not distinguish various types of isospin instabilities. Namely, in the model with the interactions with small momentum transfer all equal to V_0, the threshold for the valley polarization coincides with the Stoner threshold for intra-valley ferromagnetism and with the threshold for a charge or spin order with momentum $\mathbf{K} - \mathbf{K}'$. Indeed, performing the same calculations as we did in Sec. I, for the other two instabilities, we find that all three occur at $V_0\Pi_s = -1$. This degeneracy, however, does not hold beyond the model with a single V_0 interaction. To see this, we extend the model to two types of density-density interactions: V_0 for the density-density coupling in the same valley, and V_0' for the density-density coupling between different valleys. Evaluating the instability criteria, we find that the valley-polarization instability occurs at

$$(2V_0' - V_0)\Pi_s = -1, \tag{24}$$

while intra-valley ferromagnetic (FM) instability occurs at

$$V_0\Pi_s = -1, \tag{25}$$

and charge/spin instability with momentum $\mathbf{K} - \mathbf{K}'$ occurs at

$$V_0'\Pi_s = -1. \tag{26}$$

As a result, valley polarization is the leading instability when $V_0' > V_0$. In the opposite case $V_0 > V_0'$, the intra-valley FM is the leading instability.

The analysis at a finite field is a bit involved because once $V_0' > V_0$, valley polarization instabilities for spin-up and spin-down fermions do not decouple, i.e., there is a single instability, at which both $\chi_{v,\uparrow}$ and $\chi_{v,\downarrow}$ diverge simultaneously. The instability condition is

$$1 + V_0'(\Pi_\uparrow + \Pi_\downarrow) + \Pi_\uparrow\Pi_\downarrow V_0(2V_0' - V_0) = 0. \tag{27}$$

Still, when $|\Pi_\uparrow| > |\Pi_\downarrow|$, $\chi_{v,\uparrow} > \chi_{v,\downarrow}$, and the instability predominantly involves fermions with spin-up.

Below, we calculate the pairing vertex in the V_0-V_0' model. The bare pairing vertex in this model is V_0' because $\mathbf{k}$ and $\mathbf{k}'$ belong to different valleys. The fully dressed irreducible one at $B_\parallel = 0$ is

$$\Gamma = \frac{V_0'}{(1 - V_0\Pi)^2 - (2V_0'\Pi)^2}. \quad (28)$$

As expected, this vertex diverges at a valley polarization instability, where $(2V_0' - V_0)\Pi = -1$, but remains positive, i.e., repulsive.

At a finite field, the analysis of the pairing vertex is again more involved as the condition for the valley polarization instability does not decouple between fermions with spin-up and spin-down. Performing the calculations, we find that

$$\Gamma_{\uparrow,\uparrow} = V_0'\frac{(1 + V_0\Pi_\downarrow)^2}{Z}, \quad \Gamma_{\downarrow,\downarrow} = V_0'\frac{(1 + V_0\Pi_\uparrow)^2}{Z} \quad (29)$$

where

$$Z = (1 - V_0^2\Pi_\downarrow\Pi_\uparrow)^2 - (V_0')^2(\Pi_\downarrow + \Pi_\uparrow + 2V_0\Pi_\downarrow\Pi_\uparrow)^2 \quad (30)$$

Both $\Gamma_{\uparrow,\uparrow}$ and $\Gamma_{\downarrow,\downarrow}$ are repulsive and diverge at the valley instability at a finite $B_\parallel$, Eq. (27), as we can straightforwardly verify. Still, for $|\Pi_\uparrow| > |\Pi_\downarrow|$, $\Gamma_{\downarrow,\downarrow}$ is reduced at intermediate frequencies because of the factor $(1+V_0\Pi_\uparrow)^2$ in the numerator. It then still remains non-monotonic, at least at small $V_0'/V_0 - 1$, and allows a superconducting solution with a sign-changing gap.

VI. VALLEY-TRIPLET p-WAVE PAIRING.

The nominally repulsive valley-preserving interaction V_0 in Eq.(1) also gives rise to an attraction at a finite B in another spin-triplet channel, this time valley triplet and spatially odd. The mechanism here is the field-induced KL effect in 2D – the development of an attractive p-wave component of the static pairing interaction due to screening by particle-hole polarization bubbles. This effect has been analyzed in Refs. [60, 61]. Here we apply it to BBG.

To understand the field-induced KL effect, assume phenomenologically that the static pairing interaction $\Gamma_{ss}(0, q)$ remains proportional to valley polarization susceptibility $\chi_{v,s}$ from Eq.(5) for all $q < 2k_F$, relevant to superconductivity, and compute the polarization $\Pi_{0,s}$ explicitly. Let's do this first for a parabolic $\epsilon_i(p)$ near $\boldsymbol{K}$ and $\boldsymbol{K}'$. The result is well known: in 2D, $\Pi_s(0, q) = -(m/2\pi)$ for $q < 2k_{F,s}$ and $-(m/2\pi)\left(1 - \sqrt{4k_{F,s}^2/q^2}\right)$ for $q > 2k_{F,s}$. At $B = 0$, $k_{F,s} = k_F$ is the same for up- and down-spins. In this situation, $\Pi_s(0, q) = -m/(2\pi)$ is q-independent for relevant $q < 2K_F$, and the effective interaction $\Gamma_{ss}(0, q)$ has only an s-wave repulsive component, like the bare V_0. This is commonly known as the absence of KL effect in 2D for a parabolic dispersion [62]. The situation changes at a finite B. Now the effective interaction between majority-spin fermions comes from the minority-spin fermions and vice versa. Because the Fermi momentum $k_{F,\uparrow}$ is larger than $k_{F,\downarrow}$, there is a range $2k_{F,\downarrow} < q < 2k_{F,\uparrow}$, where the interaction $\Gamma_{\uparrow\uparrow}(0, q)$ for spin-up fermions at momentum transfer on their Fermi surface, $q < 2k_{F,\uparrow}$ acquires a momentum-dependence via the momentum dependence of $\Pi_\downarrow(0, q)$. There is no such effect for $\Gamma_{\downarrow\downarrow}(0, q)$ at $q < 2k_{F,\downarrow}$.

Once $\Gamma_{\uparrow\uparrow}(0, q)$ becomes momentum-dependent, one can search for spatially-odd solutions $\Delta(\theta)$, subject to $\int d\theta\Delta(\theta) = 0$ and $\Delta(\theta + \pi) = -\Delta(\theta)$, where θ is an angle along the Fermi surface measured from, e.g., the k_x direction. These gap functions are necessarily valley triplets. The analysis of the pairing instability is rather standard, and we just present the result. We find that the $q-$dependence of the interaction gives rise to an attraction for spatially-odd $\Delta(\theta)$. At a small $B_\parallel$ field, the gap equation is approximately local in θ and the $p-$wave transition temperature is $T_c \sim E_F e^{-1/\lambda_{KL}}$, where

$$\lambda_{KL} = \frac{mV_0}{8\pi^2\delta^2}\frac{\mu_B B}{E_F}. \quad (31)$$

At small B, T_c increases exponentially with the field. At a larger B, the prefactor gets smaller as the number of minority-spin fermions decreases. As a result, T_c has a dome-like shape as a function of B. We also note that Eq.(31) is valid when $\lambda_{KL} < 1$. At larger λ_{KL}, the coupling gets renormalized by the fermionic selfenergy and eventually saturates. The analysis can be straightforwardly extended to the physically relevant case when the instability first develops for spin-up fermions, i.e., when $\Gamma_{\uparrow\uparrow}(0, 0) \propto 1/\delta_\uparrow$ is much larger than $\Gamma_{\downarrow\downarrow}(0, 0) \propto 1/\delta_\downarrow$. One can model this by non-equal DOS for up and down spins. We found that Eq.(31) holds, but δ^2 in Eq.(31) has to be replaced by $\delta_\downarrow^2$. One can also move away from parabolic dispersion and include the q-dependence of $\Pi(0, q)$ at $q < 2k_F$. This will (i) reduce T_c and (ii) set a finite threshold on a $B_\parallel$ field as a field-induced attraction has to compete with a repulsive bare interaction in the valley-triplet channel which is activated by the q-dependence of $\Pi(0, q)$. As a result, T_c as a function of $B_\parallel$ displays a dome-like behavior above a finite threshold, much like for valley-singlet s-wave pairing. We believe that both pairing mechanisms, the s-wave discussed above and the p-wave discussed in this section, are possible in BBG, though the s-wave superconductivity is more likely to occur. This is because s-wave superconductivity does not rely on the Fermi surface shape, while our p-wave mechanism requires the Fermi surface to be nearly circular.

VII. GENERALIZATION TO SYSTEMS WITH SPIN-ORBIT INTERACTION

We argue below that the s-wave pairing mechanism also holds in systems with spin-orbit coupling (SOC). Indeed, the SOC interaction is similar in form to the Zee-

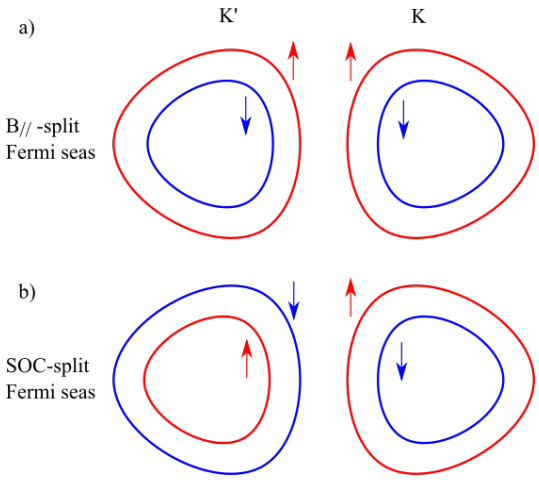

FIG. 8. Fermi seas in valleys $\boldsymbol{K}$ and $\boldsymbol{K}'$ split by a) Zeeman interaction with an external field $B_\parallel$, and b) by a spin-orbit coupling. Red (blue) arrows represent spin polarization.

man interaction with an in-plane magnetic field. Therefore, the pairing scenario in the case of SOC is linked to the one described in previous sections by interchanging the isospins. For definiteness, we consider the valley-singlet s-wave pairing. We model SOC by adding to Eq.(1) an Ising SOC:

$$H_{\rm so} = -\lambda_{\rm so}\left(\psi^\dagger_{\boldsymbol{K}\alpha}\sigma_{z,\alpha\beta}\psi_{\boldsymbol{K}\beta} - \psi^\dagger_{\boldsymbol{K}'\alpha}\sigma_{z,\alpha\beta}\psi_{\boldsymbol{K}'\beta}\right). \quad (32)$$

This term plays a role of a valley-dependent effective Zeeman field $\boldsymbol{B}_{{\rm so},\tau}$, $(\tau = K, K')$ that is directed transversely to the plane and has opposite signs for opposite valleys: $\boldsymbol{B}_{{\rm so},\boldsymbol{K}} = \frac{\lambda_{\rm so}}{\mu_B}\boldsymbol{z}$, and $\boldsymbol{B}_{{\rm so},\boldsymbol{K}'} = -\frac{\lambda_{\rm so}}{\mu_B}\boldsymbol{z}$, where $\boldsymbol{z}$ is the unit vector perpendicular to the graphene plane. As a result, the four-fold degeneracy of Fermi pockets is lifted to two sets of two-fold degenerate pockets larger ones $\boldsymbol{K}\uparrow$ and $\boldsymbol{K}'\downarrow$ and smaller ones $\boldsymbol{K}\downarrow$ and $\boldsymbol{K}'\uparrow$, see Fig.8.

Based on this observation, it is straightforward to map the scenario, described in Sec. IV, to the case of SOC – one only needs to interchange $\boldsymbol{K}'\uparrow$ and $\boldsymbol{K}'\downarrow$. Like there, we find that the electrons from smaller Fermi pockets $\boldsymbol{K}\downarrow$ and $\boldsymbol{K}'\uparrow$, experience the same non-monotonic pairing interaction as in Eq.(14), which gives rise to an s-wave valley-singlet/spin-triplet superconductivity. It is essential that the superconducting order is still robust against an in-plane magnetic field $B_\parallel\boldsymbol{x}$ and exceeds the Pauli limit [here $\boldsymbol{x}$ is a unit vector parallel to the graphene plane]. This is so because the total effective Zeeman fields in valleys $\boldsymbol{K}$ and $\boldsymbol{K}'$

$$\boldsymbol{B}_{\boldsymbol{K}} = \frac{\lambda_{\rm so}}{\mu_B}\boldsymbol{z} + B_\parallel\boldsymbol{x}, \quad \boldsymbol{B}_{\boldsymbol{K}'} = -\frac{\lambda_{\rm so}}{\mu_B}\boldsymbol{z} + B_\parallel\boldsymbol{x}, \quad (33)$$

have the same magnitudes in the presence of both $B_\parallel$ and $\lambda_{\rm so}$, so the Fermi surface degeneracy holds. The fact that $\boldsymbol{B}_{{\rm eff},\boldsymbol{K}}$ and $\boldsymbol{B}_{{\rm eff},\boldsymbol{K}'}$ are no longer parallel or anti-parallel does not matter as there is no exchange interactions between the electrons near $\boldsymbol{K}$ and $\boldsymbol{K}'$. Similarly, the analysis of valley-triplet p-wave pairing in the presence of SOC is parallel to that in Sec. VI.

VIII. RELATION TO EXPERIMENTS

We now discuss several points related to experiments. We will use existing measurements to justify our underlying assumptions and describe how our SC scenario can be tested experimentally. First, in our analysis of valley-singlet SC we assumed that isospin order sets in first for the majority-spin fermions. To verify that this interpretation of the phase transition is correct, below we calculate the slope of the phase boundary and compare it with the experiment. According to our model, instability happens only in the majority spin. Therefore, at the phase transition, the density of carriers in the majority spin is a fixed value, while the density of carriers in the minority spin depends on the $B_\parallel$ field. Specifically, we expect that the phase transition shifts towards lower total carrier density under increasing $B_\parallel$. The shift of carrier density is linear in the $B_\parallel$ field:

$$\frac{dn_*}{dB} = 2\mu_B\nu_0, \quad (34)$$

where n_* is the total carrier density at the phase boundary, μ_B is the Bohr magneton, ν_0 is the density of states per isospin, the factor of 2 arises from $\boldsymbol{K}/\boldsymbol{K}'$ valley degeneracy. Plugging in the value of the density of states obtained numerically in Ref.[21], we find the slope is $\frac{dn_*}{dB} = 5\times10^{-4}{\rm nm}^{-2}{\rm meV}^{-1}$, which matches the slope extracted from Fig.1c).

Second, as discussed above, the two scenarios for field-induced SC both yield dome-shaped $T_{\rm c}$ as a function of carrier density, with a threshold on $B_\parallel$. The only difference between the two scenarios is which spin components pair: valley-singlet pairing involves minority spins, whereas valley-triplet pairing involves majority spins. One way to test which spin components are involved in SC is to measure the DC voltage drop when injecting a spin-polarized current into the system. For instance, we can inject electrons from a ferromagnetic material that is polarized by the same in-plane magnetic field as in the BBG, then our theory predicts that for valley-singlet pairing, this spin-polarized current should give a finite DC voltage drop even when the temperature is below $T_{\rm c}$ because the SC only occurs in the Fermi sea of minority-spin electrons, while for valley-triplet pairing a DC voltage drop should disappear below $T_{\rm c}$.

Third, valley-singlet pairing arises from small-momentum (forward) scattering and thus should be sensitive to screening. Accordingly, we expect this SC to become suppressed when a proximal metal gate is introduced to screen the Coulomb interaction. On the contrary, for valley-triplet pairing, SC becomes strengthened by a proximal gate since the small-momentum scattering is harmful to this pairing channel and is strongly

screened, whereas the large-momentum (backward) scattering that helps the pairing is not so strongly screened.

Fourth, we argued that SOC plays the same role as a magnetic field and gives rise to valley-singlet s-wave or valley-triplet $p-$wave pairing. A recent experiment [22] found SC in a BBG on a monolayer of tungsten diselenide (WSe_2), a source of interfacial SOC in graphene. The observed SC develops already at zero fields and exceeds the Pauli limit in the presence of a parallel field. This fully agrees with our theory.

Finally, one might ask whether the quantum-critical mode will contribute to resistivity through carrier scattering by thermal fluctuations. While this may seem plausible at first glance, we note that the effective interaction mediated by a soft boson is strong only for small momentum transfers $q \ll k_F$. This translates into near-forward scattering processes that do not produce a current relaxation and thus do not contribute to resistivity [63]. These expectations are in line with a recent experiment [21] where resistivity T dependence shows no sign of critical fluctuations near the phase transition.

We are therefore led to conclude that all the unique aspects of the observed superconductivity are successfully explained by the attraction-from-repulsion-based pairing scenario. Furthermore, this mechanism is 'natural' as it arises from the strong electron-electron interactions that drive the adjacent isospin-polarized electron orders. As such, it constitutes a unique, verifiable instance of an exotic pairing. Supported by experiments, it sheds light on the origin of spin-triplet superconductivity in BBG and is applicable to a variety of other systems of interest.

Acknowledgments: We thank A. Young, S. Nadj-Perge, D. Efetov for sharing unpublished data, and many theory colleagues for fruitful discussions. This research was supported by the Science and Technology Center for Integrated Quantum Materials, National Science Foundation Grant No. DMR1231319, and Army Research Office Grant No. W911NF-18-1-0116. The work by A.V.C. was supported by U.S. Department of Energy, Office of Science, Basic Energy Sciences, under Award No. DE-SC0014402.

[1] Y. Cao, V. Fatemi, S. Fang, K. Watanabe, T. Taniguchi, E. Kaxiras, and P. Jarillo-Herrero, Unconventional superconductivity in magic-angle graphene superlattices, Nature **556**, 4350 (2018).

[2] X. Lu, P. Stepanov, W. Yang, M. Xie, M. A. Aamir, I. Das, C. Urgell, K. Watanabe, T. Taniguchi, G. Zhang, A. Bachtold, A. H. MacDonald, and E. Dmitri, Superconductors, orbital magnets and correlated states in magic-angle bilayer graphene, Nature **574**, 653 (2019).

[3] E. Y. Andreiand A. H. MacDonald, Graphene bilayers with a twist, Nature materials **19**, 1265 (2020).

[4] Y. Saito, J. Ge, K. Watanabe, T. Taniguchi, and A. F. Young, Independent superconductors and correlated insulators in twisted bilayer graphene, Nature Physics **16**, 926 (2020).

[5] M. Oh, K. P. Nuckolls, D. Wong, R. L. Lee, X. Liu, K. Watanabe, T. Taniguchi, and A. Yazdani, Evidence for unconventional superconductivity in twisted bilayer graphene, Nature **600**, 240 (2021).

[6] Y. Cao, D. Rodan-Legrain, J. M. Park, N. F. Q. Yuan, K. Watanabe, T. Taniguchi, R. M. Fernandes, L. Fu, and P. Jarillo-Herrero, Nematicity and competing orders in superconducting magic-angle graphene, Science **372**, 264 (2021).

[7] A. Jaoui, I. Das, G. Di Battista, J. Díez-Mérida, X. Lu, K. Watanabe, T. Taniguchi, H. Ishizuka, L. Levitov, and D. K. Efetov, Quantum critical behaviour in magic-angle twisted bilayer graphene, Nature Physics **18**, 633638 (2022).

[8] R. Bistritzerand A. H. MacDonald, Moiré bands in twisted double-layer graphene, Proceedings of the National Academy of Sciences **108**, 12233 (2011).

[9] L. Balents, C. R. Dean, D. K. Efetov, and A. F. Young, Superconductivity and strong correlations in moiré flat bands, Nature Physics **16**, 725 (2020).

[10] X. Liu, Z. Wang, K. Watanabe, T. Taniguchi, O. Vafek, and J. Li, Tuning electron correlation in magic-angle twisted bilayer graphene using coulomb screening, Science **371**, 1261 (2021).

[11] Y.-Z. Youand A. Vishwanath, Superconductivity from valley fluctuations and approximate SO(4) symmetry in a weak coupling theory of twisted bilayer graphene, npj Quantum Materials **4**, 1 (2019).

[12] V. Kozii, H. Isobe, J. W. F. Venderbos, and L. Fu, Nematic superconductivity stabilized by density wave fluctuations: Possible application to twisted bilayer graphene, Phys. Rev. B **99**, 144507 (2019).

[13] D. V. Chichinadze, L. Classen, and A. V. Chubukov, Nematic superconductivity in twisted bilayer graphene, Phys. Rev. B **101**, 224513 (2020).

[14] E. Khalaf, S. Chatterjee, N. Bultinck, M. P. Zaletel, and A. Vishwanath, Charged skyrmions and topological origin of superconductivity in magic-angle graphene, Science advances **7**, eabf5299 (2021).

[15] Y. Saito, J. Ge, K. Watanabe, T. Taniguchi, and A. F. Young, Decoupling superconductivity and correlated insulators in twisted bilayer graphene, arXiv preprint arXiv:1911.13302 (2019).

[16] P. Stepanov, I. Das, X. Lu, A. Fahimniya, K. Watanabe, T. Taniguchi, F. H. Koppens, J. Lischner, L. Levitov, and D. K. Efetov, Untying the insulating and superconducting orders in magic-angle graphene, Nature **583**, 375 (2020).

[17] F. Wu, A. H. MacDonald, and I. Martin, Theory of phonon-mediated superconductivity in twisted bilayer graphene, Phys. Rev. Lett. **121**, 257001 (2018).

[18] B. Lian, Z. Wang, and B. A. Bernevig, Twisted bilayer graphene: A phonon-driven superconductor, Phys. Rev. Lett. **122**, 257002 (2019).

[19] F. Wu, E. Hwang, and S. Das Sarma, Phonon-induced giant linear-in-t resistivity in magic angle twisted bilayer

graphene: Ordinary strangeness and exotic superconductivity, Phys. Rev. B **99**, 165112 (2019).
[20] G. Tarnopolsky, A. J. Kruchkov, and A. Vishwanath, Origin of magic angles in twisted bilayer graphene, Phys. Rev. Lett. **122**, 106405 (2019).
[21] H. Zhou, L. Holleis, Y. Saito, L. Cohen, W. Huynh, C. L. Patterson, F. Yang, T. Taniguchi, K. Watanabe, and A. F. Young, Isospin magnetism and spin-polarized superconductivity in bernal bilayer graphene, Science **375**, 774 (2022).
[22] Y. Zhang, R. Polski, A. Thomson, É. Lantagne-Hurtubise, C. Lewandowski, H. Zhou, K. Watanabe, T. Taniguchi, J. Alicea, and S. Nadj-Perge, Enhanced superconductivity in spinorbit proximitized bilayer graphene, Nature 613, 268273 (2023).
[23] H. Zhou, T. Xie, A. Ghazaryan, T. Holder, J. R. Ehrets, E. M. Spanton, T. Taniguchi, K. Watanabe, E. Berg, M. Serbyn, and et al., Half- and quarter-metals in rhombohedral trilayer graphene, Nature **598**, 429433 (2021).
[24] H. Zhou, T. Xie, T. Taniguchi, K. Watanabe, and A. F. Young, Superconductivity in rhombohedral trilayer graphene, Nature **598**, 434 (2021).
[25] A. Klein, A. V. Chubukov, Y. Schattner, and E. Berg, Normal state properties of quantum critical metals at finite temperature, Phys. Rev. X **10**, 031053 (2020).
[26] V. Oganesyan, S. A. Kivelson, and E. Fradkin, Quantum theory of a nematic fermi fluid, Phys. Rev. B **64**, 195109 (2001).
[27] S. Lederer, Y. Schattner, E. Berg, and S. A. Kivelson, Enhancement of superconductivity near a nematic quantum critical point, Phys. Rev. Lett. **114**, 097001 (2015).
[28] A. M. S. Tremblay, Strongly correlated superconductivity (2013), arXiv:1310.1481 [cond-mat.supr-con].
[29] A. V. Chubukov, A. Abanov, Y. Wang, and Y.-M. Wu, The interplay between superconductivity and non-fermi liquid at a quantum-critical point in a metal, Annals of Physics **417**, 168142 (2020), Eliashberg theory at 60: Strong-coupling superconductivity and beyond.
[30] E. Berg, S. Lederer, Y. Schattner, and S. Trebst, Monte carlo studies of quantum critical metals, Annual Review of Condensed Matter Physics **10**, 63 (2019).
[31] S.-S. Lee, Recent developments in non-fermi liquid theory, Annual Review of Condensed Matter Physics **9**, 227 (2018).
[32] K. B. Efetov, H. Meier, and C. Pepin, Pseudogap state from quantum criticality, Nature Physics **9**, 442 (2013).
[33] P. Monthoux, D. Pines, and G. G. Lonzarich, Superconductivity without phonons, Nature **450**, 1177 (2007).
[34] I. I. Mazin, D. J. Singh, M. D. Johannes, and M. H. Du, Unconventional superconductivity with a sign reversal in the order parameter of $LaFeAsO_{1-x}F_x$, Phys. Rev. Lett. **101**, 057003 (2008).
[35] I. Mazinand J. Schmalian, Pairing symmetry and pairing state in ferropnictides: Theoretical overview, Physica C: Superconductivity **469**, 614 (2009), superconductivity in Iron-Pnictides.
[36] A. Abanov, A. V. Chubukov, and J. Schmalian, Quantum-critical theory of the spin-fermion model and its application to cuprates: Normal state analysis, Advances in Physics **52**, 119 (2003).
[37] W. Qin, C. Huang, T. Wolf, N. Wei, I. Blinov, and A. H. MacDonald, Functional renormalization group study of superconductivity in rhombohedral trilayer graphene, arXiv:2203.09083 (2022).
[38] A. Ghazaryan, T. Holder, M. Serbyn, and E. Berg, Unconventional superconductivity in systems with annular fermi surfaces: Application to rhombohedral trilayer graphene, Phys. Rev. Lett. **127**, 247001 (2021).
[39] Y.-Z. Chou, F. Wu, J. D. Sau, and S. Das Sarma, Acoustic-phonon-mediated superconductivity in bernal bilayer graphene, Phys. Rev. B **105**, L100503 (2022).
[40] P. Moreland P. W. Anderson, Calculation of the superconducting state parameters with retarded electron-phonon interaction, Phys. Rev. **125**, 1263 (1962).
[41] W. L. McMillan, Transition temperature of strong-coupled superconductors, Phys. Rev. **167**, 331 (1968).
[42] N. N. Bogoljubov, V. V. Tolmachov, and D. V. irkov, A new method in the theory of superconductivity, Fortschritte der Physik **6**, 605 (1958).
[43] P. Coleman, Introduction to many-body physics (Cambridge University Press, 2015).
[44] J. Ruhmanand P. A. Lee, Superconductivity at very low density: The case of strontium titanate, Phys. Rev. B **94**, 224515 (2016).
[45] A. Chubukov, N. V. Prokof'ev, and B. V. Svistunov, Implicit renormalization approach to the problem of Cooper instability, Phys. Rev. B **100**, 064513 (2019).
[46] D. Pimenovand A. V. Chubukov, Quantum phase transition in a clean superconductor with repulsive dynamical interaction, npj Quantum Materials **7**, 1 (2022).
[47] W. Kohnand J. M. Luttinger, New mechanism for superconductivity, Phys. Rev. Lett. **15**, 524 (1965).
[48] J. Jung, F. Zhang, and A. H. MacDonald, Lattice theory of pseudospin ferromagnetism in bilayer graphene: Competing interaction-induced quantum hall states, Phys. Rev. B **83**, 115408 (2011).
[49] E. McCannand M. Koshino, The electronic properties of bilayer graphene, Reports on Progress in physics **76**, 056503 (2013).
[50] Z. Dong, M. Davydova, O. Ogunnaike, and L. Levitov, Isospin-and momentum-polarized orders in bilayer graphene, Physical Review B **107**, 075108 (2023).
[51] Z. Dongand L. Levitov, Superconductivity in the vicinity of an isospin-polarized state in a cubic dirac band, arXiv preprint arXiv:2109.01133 (2021).
[52] D. V. Chichinadze, L. Classen, Y. Wang, and A. V. Chubukov, Su(4) symmetry in twisted bilayer graphene: An itinerant perspective, Phys. Rev. Lett. **128**, 227601 (2022).
[53] A. V. Chubukovand P. Wölfle, Quasiparticle interaction function in a two-dimensional fermi liquid near an antiferromagnetic critical point, Phys. Rev. B **89**, 045108 (2014).
[54] D. Chowdhury, A. Georges, O. Parcollet, and S. Sachdev, Sachdev-ye-kitaev models and beyond: Window into non-fermi liquids, Rev. Mod. Phys. **94**, 035004 (2022).
[55] P. A. Lee, Gauge field, aharonov-bohm flux, and high-T_c superconductivity, Phys. Rev. Lett. **63**, 680 (1989).
[56] B. Blokand H. Monien, Gauge theories of high-Tc superconductors, Phys. Rev. B **47**, 3454 (1993).
[57] C. Nayakand F. Wilczek, Non-fermi liquid fixed point in 2 + 1 dimensions, Nuclear Physics B **417**, 359 (1994).
[58] B. L. Altshuler, L. B. Ioffe, and A. J. Millis, Low-energy properties of fermions with singular interactions, Phys. Rev. B **50**, 14048 (1994).
[59] Y. B. Kim, A. Furusaki, X.-G. Wen, and P. A. Lee, Gauge-invariant response functions of fermions coupled

to a gauge field, Phys. Rev. B **50**, 17917 (1994).
[60] A. Chubukovand M. Kagan, Increase in superconducting temperature in polarized fermi gas with repusion, JETP Letters **50**, 517 (1989).
[61] S. Raghuand S. A. Kivelson, Superconductivity from repulsive interactions in the two-dimensional electron gas, Phys. Rev. B **83**, 094518 (2011).
[62] M. Baranovand M. Y. Kagan, Superconductivity in a low-density two-band model with a repulsive interaction: extended analysis, J. Exp. Theor. Phys **75**, 165 (1992).
[63] D. L. Maslov, V. I. Yudson, and A. V. Chubukov, Resistivity of a non-galilean–invariant fermi liquid near pomeranchuk quantum criticality, Phys. Rev. Lett. **106**, 106403 (2011).

Appendix A: Self-energy and superconductivity

In this section, we elaborate on the effect of self-energy correction and show that it has a marginal impact on superconductivity. Here, we focus on the case of $\nu_1 = 0$. The self-energy for spin-down electrons is given by

$$\begin{aligned}\Sigma_{\downarrow\downarrow}(\omega) &= \int \frac{d\nu}{2\pi}\int \frac{dq_\perp}{2\pi}\frac{\overline{\Gamma}_{\downarrow\downarrow}(\nu,q)}{i(\omega+\nu)-v_F q_\perp} \\ &= \frac{\lambda}{2}\int \frac{d\nu}{2\pi}\mathrm{sgn}(\nu+\omega)S(\nu/\nu_0) \\ &= \lambda\nu_0\int_0^{\bar{\omega}} dx S(x)\end{aligned} \tag{A1}$$

To see the relevant scale of ω in the pairing problem, we look at the gap equation without self-energy correction Eq.(23). We rewrite it as follows:

$$\Delta(n) = -\frac{\lambda}{2}\sum_{n'}\frac{\Delta(n')}{|2n'+1|}S\left(2\pi\bar{T}_c\left(n-n'\right),0\right) \tag{A2}$$

where we have rewritten $\bar{\omega} = \pi(2n+1)\bar{T}_\mathrm{c}$, $\bar{\omega}' = \pi(2n'+1)\bar{T}_\mathrm{c}$. As shown by numerics in the main text, the critical temperature is $T_\mathrm{c} \sim \frac{1}{2}\lambda\nu_0 \times 10^{-2}$. For extremely large value of $\lambda \gg 10^2$ (i.e. extremely small $\delta_\downarrow$), the relevant $n, n' \sim O(1)$. Replacing $S(x)$ with its asymptotic form $\frac{1}{2x}$, we find numerically that the wavefunction stop changing sign at $n = 4$. The self-energy relevant for this pairing problem should be evaluated at $\omega = 9\pi T_\mathrm{c}$:

$$\Sigma_{\downarrow\downarrow}(\omega \sim 9\pi T_\mathrm{c}) \sim \lambda\nu_0 \ln(\lambda) \tag{A3}$$

where logarithm comes from integrating $S(x)$ which scales as $\frac{1}{2x}$ at large x. Then, we find the effective coupling scales with λ as

$$\tilde{\lambda} = \frac{\lambda}{1+\kappa\ln\lambda}, \quad \kappa \sim \frac{100}{9\pi} = 3.5 \tag{A4}$$

The denominator is only marginally relevant at large λ, thus does not suppress the T_c substantially.

For a not-so-large λ value ($\lambda < 10^2$), the relevant value of n, n' the equation above is $n, n' \lesssim \nu_0/T_\mathrm{c} = 10^2/\lambda$. The self-energy relevant for this pairing problem should be evaluated at $\omega \lesssim \nu_0$:

$$\Sigma_{\downarrow\downarrow}(\omega \sim \nu_0) \sim 0.2\lambda\nu_0 \tag{A5}$$

where the numerical factor comes from integrating $S(x)$ below the turning pint $x \sim 0.5$. We find the effective coupling scales with λ as

$$\tilde{\lambda} = \frac{\lambda}{1+0.2\lambda}. \tag{A6}$$

In this case, carrying out the simulation as in the main text [see Fig.7 and accompanying discussion], we get $T_\mathrm{c} \sim 10^{-4}E_F$. This value is much smaller than the ones in Fig.7 but still of an acceptable order of magnitude.